Influence of Zr addition on the microstructures and mechanical properties of 14Cr ODS steels

Liye Zhang[a], Liming Yu[a],[*], Yongchang Liu[a], Chenxi Liu[a], Huijun Li[a], Jiefeng Wu[b]

[a] State Key Lab of Hydraulic Engineering Simulation and Safety, Tianjin key Lab of Composite and Functional Materials, Tianjin University, Tianjin 300072, China
[b] Institute of Plasma Physics, Chinese Academy of Sciences, Hefei 230031, China

ARTICLE INFO

ABSTRACT

Oxide dispersion strengthened (ODS) steel is one of the most promising candidate structural materials for the high-temperature nuclear reactor application. In this study, two compositions of ODS steels (14Cr-ODS and 14Cr-Zr-ODS) were prepared to investigate the influence of Zr addition on the microstructures and mechanical properties of ODS steels. The microstructures, including dispersion morphology and crystal structures of oxide particles, particle-matrix interface coherency and particle-dislocation interactions, were characterized using TEM, HRTEM, and SEM, and the mechanical properties at room and high temperatures were measured using uniaxial tensile tests. Results show that Zr addition leads to the formation of finer precipitated particles, which was identified as rhombohedral $Y_4Zr_3O_{12}$, with denser dispersion in the matrix. The calculation results reveal that the lattice misfit, δ, at the interface between particle and matrix increases as the particle size increases. In addition, the strength and elongation of ODS steels are improved with Zr addition due to the stronger interface bonding force between fine particles and matrix as well as the larger pinning effect of small particles to dislocation movements.

1. Introduction

The structural components of future fusion reactors will be subjected to high heat loads and neutron fluxes [1]. New structural materials are needed to provide engineering solutions for such severe conditions [2]. Many different types of high-temperature structural materials, including austenitic stainless steel, ferritic/martensitic stainless steel and nickel-base alloy have been used in nuclear reactors in the past few years. Although these alloys can maintain good mechanical properties at high temperature, they are not able to resist void swelling under the neutron irradiation [3,4]. In recent years, oxide dispersion strengthened (ODS) steels have become the most promising candidate materials among those steels for the similar applications [2,5]. The ODS steels were designed to withstand both high heat loads and neutron fluxes by the dispersion strengthening mechanism, in which nano-sized and highly stable precipitated oxide particles are uniformly distributed throughout the matrix [6]. Acting as the structural material of the reactors, ODS steels play a critical role in the development of nuclear engineering. Therefore, it has become a hot topic for researchers to further improve the mechanical characteristics of ODS steels.

It is commonly known that the outstanding characteristics of the material depend not only on the advanced preparation and processing

technologies but also on proper composition designs. In the early stage of the ODS steels development, the oxide particles were pure Y_2O_3 with large size and simple crystal structure. These characteristics cannot meet the requirements for strengthening. Although the nanoparticles can be optimized by adding Ti element subsequently, the performances were still not ideal. Recently, more and more studies have focused on modifying the compositions of ODS steels by adding Al, Zr, Hf, and other elements [7–10]. Experimental results have proven that Al addition can improve the corrosion resistance of ODS steels by forming a layer of dense oxide film in the surface. However, the formation of Y-Al-O phase would result in a prominent coarsening effect on the oxide particles, and the portion of Al dissolved in the matrix could also deteriorate the strength. For Zr element, the first principles calculation results indicate that the binding energy of the Y-Zr-O cluster is much higher than that of the Y-Ti-O and Y-Al-O clusters in the Fe matrix, which indicates that the Y-Zr-O phase is easier to form and remains more stable than the Y-Ti-O and Y-Al-O phases [11,12]. In addition, Yu et al. [13] and Ohnuki et al. [14] have also detected complex Y-Zr-O oxides particles which have smaller sizes and higher number density in high-Cr ODS steels with Zr addition. In fact, the optimized effect of Hf on the microstructure of ODS steels is similar to Zr, because both of them are in the same subgroup in the periodic table. But Hf is not an

---

ideal selection for the structural materials application in nuclear power plant since Hf has a longer decay time than Zr after irradiation. It can be expected that Zr addition is a more appropriate choice to improve the microstructures of ODS steels, especially in the nuclear reactor application. However, the further information about these particles in Zr-contained ODS steels and the influence of Zr addition on the mechanical properties of ODS steels are still not clear. Therefore, more in-depth researches on the optimization mechanism of Zr addition on the microstructures and mechanical properties of ODS steels are necessary.

In this paper, two compositions of ODS steels with and without Zr addition were prepared to investigate the influence of Zr on the microstructure and the mechanical properties at various temperatures. The differences in the crystal structures of the precipitated oxide particles, the particle-matrix orientation relationships and the interface coherency, as well as the mechanical performances due to the Zr addition are characterized and analyzed.

2. Materials and experimental details

Two compositions of nitrogen-gas-atomized powders with and without Zr element were mixed with 0.45 wt% nano-sized Y_2O_3 powders. The mixed powders were mechanical alloyed in a QM-2SP12 high-energy planetary ball mill with the same parameters (the ball-to-powder weight ratio of 10:1, rotation speed of 250 rpm, and total milling time of 30 h) under pure argon protective atmosphere, respectively. Subsequently the as-milled powders were consolidated by hot isostatic pressing (HIP) at 1150 ℃ under a pressure of 150 MPa for 3 h. The as-HIPed samples were annealed at 1050 ℃ for 1.5 h. Table 1 shows the compositions of the two contrast samples.

The microstructures , especially the morphology and coherency of oxide particles, were investigated by transmission electron microscopy (TEM), high resolution transmission electron microscopy (HRTEM) and X-ray energy dispersive spectroscopy (EDS) using a JEM-2100F operating at 200 kV. The thin foil samples used for TEM were mechanically thinned to 50 μm and punched into 3 mm discs, and then electropolished with 5% perchloric acid and 95% alcohol at −30 ℃ using a MTA-1A twin jet polisher. The standard uniaxial tensile tests were carried out at room temperature and different high temperatures (300 ℃, 550 ℃ and 750 ℃) with a strain rate of 1 mm/min. Three tensile samples of each composition were tested at each temperature. The shape and size of the tensile samples is shown in Fig. 1. The fractured section surface of tensile samples was observed by scanning electron microscope (SEM).

3. Results and discussion

3.1. Microstructure analyses

3.1.1. Morphology and composition of particles
The effect of Zr addition on the morphology, the crystal structure and the composition of the nanoclusters in the two ODS alloys were investigated by TEM and HRTEM. The bright field images of the oxide particles dispersed in the matrix of the 14Cr-ODS and 14Cr-Zr-ODS are shown in Fig. 2(a) and (b), respectively. It is seen that almost all of the oxide particles in two steels maintain their spherical shapes. The particle size frequency distribution histogram and the Gause fitting curves of the two alloys are shown in Fig. 2(c), and their corresponding statistical results of the size and distribution characteristic parameters calculated from more than 200 particles for each sample are summar-

Table 1
Nominal composition (wt%) of the two samples.

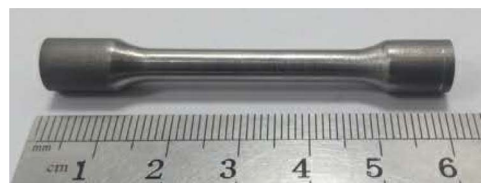|	Fe	Cr	W	Zr	Y_2O_3
14Cr-ODS	Bal.	14	1.5	—	0.45
14Cr-Zr-ODS	Bal.	14	1.5	0.90	0.45

Fig. 1. The shape and size of the samples used for tensile tests.

ized in Table 2. The main differences between two samples are that the particles in the 14Cr-Zr-ODS matrix exhibit a smaller mean diameter, shorter inter-particle spacing, higher number density and volume fraction than those of the 14Cr-ODS. Additionally, the particle size distribution in the 14Cr-Zr-ODS is more concentrated than that in the 14Cr-ODS since some particles in the latter steel are extremely large with sizes even up to 30–35 nm. Therefore, adding Zr can not only reduce the precipitated particle size and inter-particle spacing but also increase the number density of the particles.

The composition and crystal structure of the particles in 14Cr-Zr-ODS alloy were investigated by HRTEM method and the results were evaluated using fast Fourier transformation (FFT). The high-resolution image of a typical particle in 14Cr-Zr-ODS with a diameter of 8.5 nm was shown in Fig. 3(a) and the corresponding FFT result and the indexes of diffraction spots were shown in Fig. 3(b) and (c), respectively. The average atomic ratio Y:Zr of the particles is roughly 1.3 based on the EDS analysis. The inter-planar distances measured from the reciprocal space in Fig. 3(c) are consistent with the database table for rhombohedral $Y_4Zr_3O_{12}$ based on the powder diffraction pattern, as shown in Table 3 (the electron beam is paralleled to $[2\bar{1}0]$ zone axis of this particle). Moreover, as indicated in Fig. 3(a), the atomic plane spacing of the lattice fringes from {003} and {121} and the angle between them are also consistent with the database table. The $Y_4Zr_3O_{12}$ oxide has a space group of R-3(148) with $a=b=0.9734$ nm and $c=0.9109$ nm, $\alpha=\beta=90°$, and $\gamma=120°$. Other two randomly selected particles with similar sizes, 7.1 nm and 9.8 nm, were also identified and the results were also consistent with the database table for the $Y_4Zr_3O_{12}$. This structure is a derivative of the fluorite structure ZrO_2, which reveals the occurrence of internal oxidation reactions: $2Y_2O_3+3ZrO_2 \rightarrow Y_4Zr_3O_{12}$ during the consolidation due to the affinity of oxygen to solute atoms [15,16].

A larger particle with a diameter of 14.1 nm in 14Cr-Zr-ODS alloy was also investigated. As shown in Fig. 4 and Table 4, it was identified as monoclinic Y_2O_3 particles. Table 4 shows the relevant database, the electron beam is paralleled to $[1\bar{1}0]$ zone axis of the particle.

Several randomly selected particles in 14Cr-Zr-ODS with different diameters were studied by HRTEM and FFT method. It was found that the precipitated particles with relatively smaller sizes tend to be the $Y_4Zr_3O_{12}$ while the particles with relatively larger sizes generally exist as Y_2O_3.

3.1.2. Particle-matrix coherency and interface structures
The following work focuses on the coherency relationship of oxide particles in 14Cr-Zr-ODS with the Fe-Cr ferritic matrix, which may contribute to a further understanding of the strengthening mechanism of Zr addition. The coherency of the oxide particles with the matrix can be evaluated based on the Ashby-Brown contrast method [17]. According to Refs. [16,18], most precipitated particles can be divided into three groups: lobe-lobe contrast, black/white dot contrast and oxide particles with no-contrast lines (also called Moiré fringes, MF). Among them, both lobe-lobe contrast and dot contrast indicate that the particle is coherent with the surrounding matrix. The difference between them is that, the particle will be seen as the former contrast if it lies close to the surface of TEM foil and as the later contrast if it lies in the center of the foil. Particles with no-contrast lines perpendicular to the active vector **g** are semi-coherent with the matrix. Fig. 5 shows that all three kinds of contrasts can be observed in most of the oxide particles in
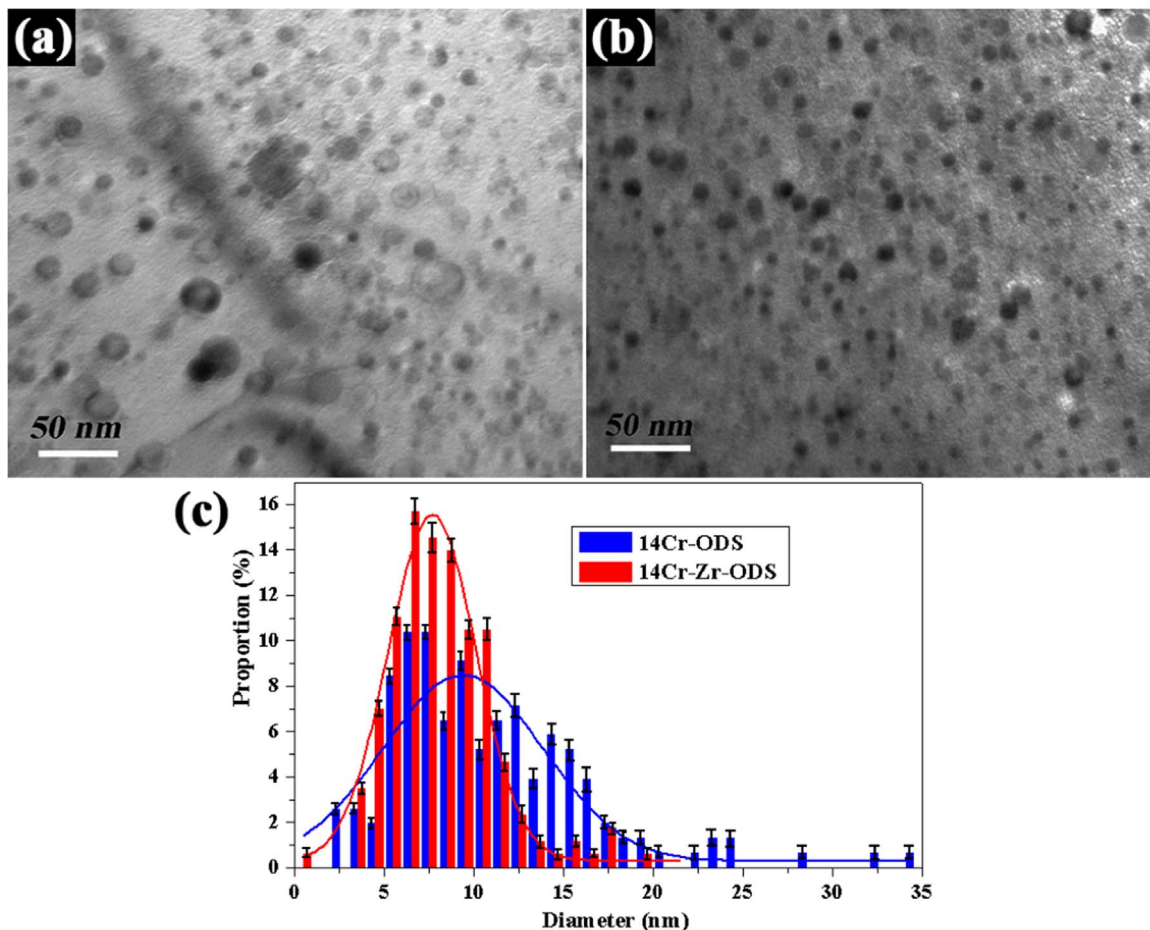
Fig. 2. TEM bright field images of oxide particles morphology, respectively for (a) 14Cr-ODS and (b)14Cr-Zr-ODS; (c) particle size frequency distribution histogram and the Gause fitting curves of this two alloys.

Table 2
The statistical results of particles morphology in the two samples.

	Mean diameter (nm)	Maximum diameter (nm)	Inter-particle spacing (nm)	Number density (m^{-2})	Volume fraction	Most probable distribution of particle sizes (nm)
14Cr-ODS	10.91	34.28	24.07	1.54×10^{15}	0.416%	6–17
14Cr-Zr-ODS	8.19	19.97	17.54	2.31×10^{15}	0.535%	4–11

14Cr-Zr-ODS alloy, indicating that they are coherent or semi-coherent with the matrix.

We now turn to discuss and calculate the details of interface coherency relationships and the misfit δ. The formation mechanism of Moiré fringes can be illustrated as follows: if a lattice plane of a particle is paralleled and perfectly matched with a plane of the matrix

(perpendicular to the active **g** vector), the lattice distortion along the **g** vector will be zero, which means the misfit strain field does not have any component on the lattice plane parallel to the **g** vector, and that the beam intensity distribution becomes the same with that for a perfect matrix crystal. In this case, a Moiré fringe will appear at the position of this pair of perfectly matched planes [19,20]. Due to the existence of
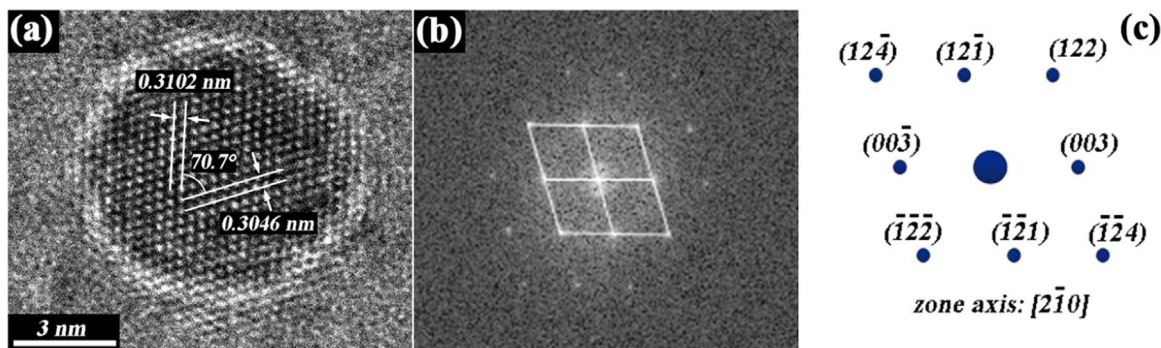

Fig. 3. (a) HRTEM image of an $Y_4Zr_3O_{12}$ particle with diameter of 8.5 nm; (b) FFT image obtained from (a); (c) indexes of diffraction spots in (b).

Table 3

Comparison between measured inter-planar distances and the theoretical values in database of $Y_4Zr_3O_{12}$.

Crystal face index	{12-1}	{122}	{003}	{−1−24}
Theoretical inter-planar distance (nm)	0.2997	0.2611	0.3026	0.1852
Measured inter-planar distance (nm)	0.2964	0.2593	0.3096	0.1888

Table 4

Comparison between measured inter-planar distances and the theoretical values in database of Y_2O_3.

Crystal face index	{003}	{112}	{11-1}
Theoretical inter-planar distance (nm)	0.2824	0.2589	0.3097
Measured inter-planar distance (nm)	0.2907	0.2574	0.3023

lattice misfit between the parallel planes of particle and matrix, a misfit dislocation must be formed to release the misfit strain for every $1/\delta$ planes. Obviously, the distance of $1/\delta$ planes is just equal to the inter-spacing of two neighbouring Moiré fringes (D_{MF}). So the misfit δ can be roughly calculated by:

$$\delta \approx \frac{d_{Oxide}(\text{or} d_{Matrix})}{D_{MF}}, \tag{1}$$

in which d_{Oxide} and d_{Matrix} represent the inter-planar distances of oxide and matrix respectively. In order to calculate the misfit δ of particles with different sizes, four typical particles with diameters of about 4 nm, 6 nm, 11.5 nm and 14 nm were characterized by HRTEM, FFT, and IFFT (inverse fast Fourier transformation). Among them, the two smaller sized particles of 4 nm and 6 nm were identified as $Y_4Zr_3O_{12}$, while the larger particles of 11.5 nm and 14 nm were identified as Y_2O_3.

Fig. 6 shows the HRTEM micrograph of a small $Y_4Zr_3O_{12}$ particle with diameter of 4 nm which was taken under **g**(110). It is clear that the particle exhibits a dot contrast. The clear lattice fringes of both particle and matrix indicate that they are well coherent under the direction of **g**. According to Eq. (1), the inter-spacing of Moiré fringes (D_{MF}) increases as the misfit (δ) decreases. For this coherent small particle, the D_{MF} is much larger than the size of particle ($D_{Particle}$) due to the very small δ. So that no Moiré fringe can actually be formed on the particle. According to the fact of $D_{MF} > D_{Particle}$ and the measured values of $d(110)_{Matrix}$ (0.202 nm) and $D_{Particle}$ (4.01 nm), the misfit of this particle can be determined as $\delta < d_{Matrix}/D_{Particel} = 5.03\%$.

Another small particle with diameter of about 6 nm taken under **g** (110) was shown in Fig. 7(a). This $Y_4Zr_3O_{12}$ particle is also well coherent with the surrounding matrix by observing the clear lattice fringes directly. According to the measured values of D_{MF} (2.1 nm) and $d(110)_{Matrix}$ (0.201 nm), the misfit of this particle is $\delta \approx d_{Matrix}/D_{MF} = 9.57\%$. The inverse fast Fourier transformation (IFFT) image (shown in Fig. 7(b)), taken from the interface area covered by white square in Fig. 7(a), shows that there was a misfit dislocation formed in the particle, indicating that the d_{Oxide} is slightly smaller than d_{Matrix}. Thus the detailed interface lattice structure can be illustrated by the schematic diagram shown in Fig. 7(c). The orientation relationship is $(410)_{Y4Zr3O12}\|(110)_{Matrix}$.

A large particle, which was identified as Y_2O_3, with diameter of 11.5 nm taken under **g**(200) was shown in Fig. 8(a). In this particle, the Moiré fringes were distributed densely, indicating the relatively large misfit of the particle. In this case, the inter-planar spacing numerical difference between the particle and matrix is relatively large. The δ
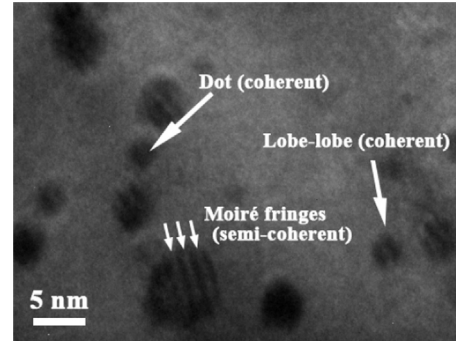

Fig. 5. TEM image of particles in 14Cr-Zr-ODS alloy at high magnification.
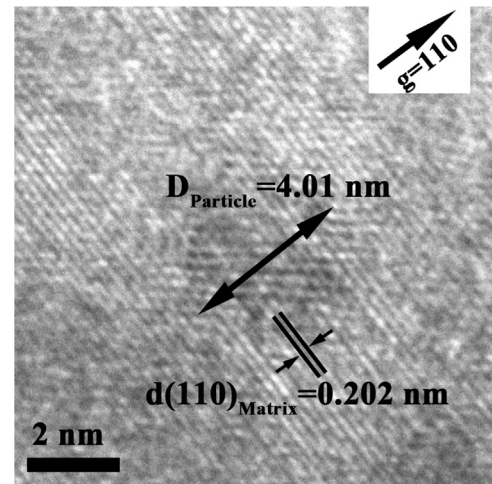

Fig. 6. HRTEM micrograph of a small $Y_4Zr_3O_{12}$ particle with diameter of 4 nm.

calculated method should be revised as:

$$\delta \approx \frac{d_{Oxide} + d_{Matrix}}{2D_{MF}} \tag{2}$$

and the accuracy of Eq. (2) can be checked by Eq. (3) according to the definition of misfit:

$$\delta = \frac{2|d_{Oxide} - d_{Matrix}|}{(d_{Oxide} + d_{Matrix})} \tag{3}$$
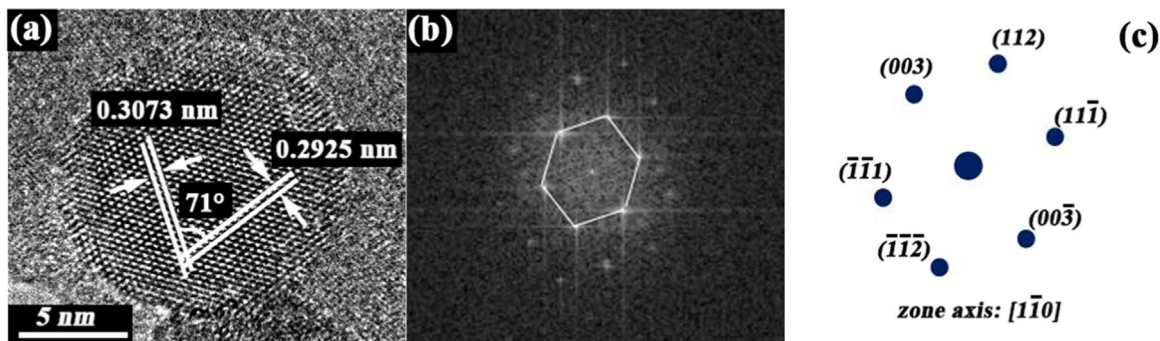

Fig. 4. (a) HRTEM image of an Y_2O_3 particle with diameter of 14.1 nm, (b)FFT image obtained from (a), (c) indexes of diffraction spots in (b).
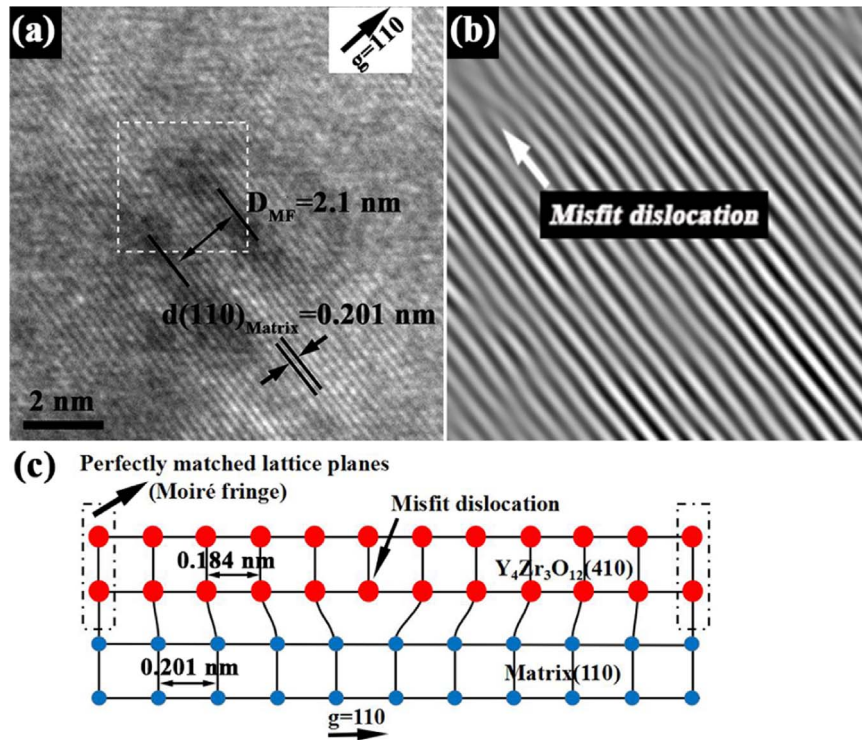
Fig. 7. (a) HRTEM micrograph of a small Y$_4$Zr$_3$O$_{12}$ particle with diameter of 6 nm; (b) IFFT image of the area covered by white square in (a); (c) schematic diagram of the interface structure for this particle.

Here d_{Oxide} and D_{MF} were measured as 0.338 nm and 1.327 nm respectively. The d_{Matrix} was measured by FFT method. It is worth noting that the measured distance (0.27 nm) by diffraction spots is about twice that of the inter-planar spacing of $d(200)_{Matrix}$ due to the condition of structural extinction. Therefore, this kind of interface structure can be illustrated by the schematic diagram shown in Fig. 8(b). Here the d_{Matrix} in Eqs. (2) and (3) should be replaced by $2d(200)_{Matrix}$ in order to calculate the misfit. Finally, δ calculated by Eqs. (2) and (3) were 22.9% and 22.3% respectively. The orientation relationship of this particle is $(202)_{Y2O3}\|(200)_{Matrix}$.

Another more larger Y$_2$O$_3$ particle with a diameter of 14 nm taken under **g**(200) was shown in Fig. 9(a). The most significant feature of this particle, compared with the previous one, is that the Moiré fringes are not parallel to the crystal faces and there is an included angle between them. This indicates that $(202)_{Y2O3}$ is not completely parallel to $(200)_{Matrix}$. According to the equation $\varphi = tg^{-1}\frac{T_1 \sin\theta}{T_1\cos\theta - T_2}$ (where θ is the included angle between the lattice planes of particle and matrix; φ is the included angle of Moiré fringes; T_1 and T_2 is the diffraction period of matrix and particle respectively) in Ref. [21], a minuscule change of θ will cause a notable change of φ, and θ has opposite sign with φ when

$T_1 < T_2$. The enlarged view of the FFT image shown in Fig. 9(c) verifies this phenomenon. Therefore the interface structure of the particle can be illustrated by the schematic diagram shown in Fig. 9(b). The d_{Matrix} in Eqs. (2), (3) should be replaced by $2d(200)_{Matrix}\cos\theta$ in order to calculate the misfit. θ and φ measured by FFT was 0.66° and 7.02° respectively. In this case, δ calculated by Eqs. (2) and (3) were 25.4% and 25.8% respectively.

According to the above calculated results, as listed in Table 5, the relatively small particles are well coherent with matrix with smaller misfit. As the particle size increases, the misfit becomes larger. When the particle size reaches about 14 nm, the crystal planes of the particle and matrix in the direction of **g** will no longer be paralleled completely.

3.2. Mechanical properties researches

3.2.1. Comparison of mechanical properties

Three replicate tensile tests were performed for each composition of the ODS steel at each temperature. All the stress-strain curves of 14Cr-ODS and 14Cr-Zr-ODS tested at room temperature are shown in Fig. 10. And the average stress-strain curves of every three replicate samples
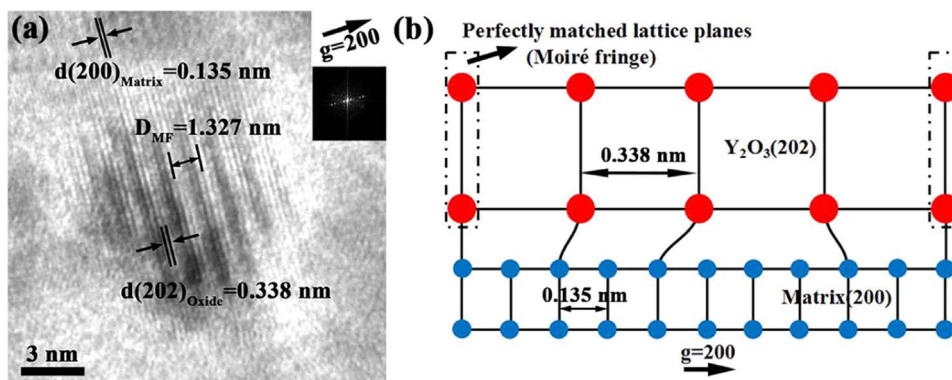

Fig. 8. (a) HRTEM micrograph of a large Y$_2$O$_3$ particle with diameter of 11.5 nm; (b) schematic diagram of the interface structure for this particle.
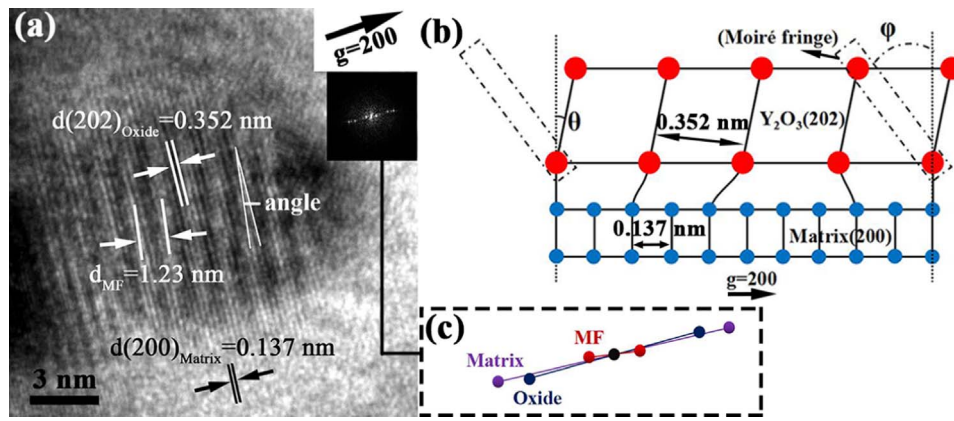
Fig. 9. (a) HRTEM micrograph of a large Y_2O_3 particle with diameter of 14 nm; (b) simple schematic diagrams of the interface structure for this particle; (c) enlarged view of the FFT image in (a).

Table 5
The lattice misfit δ list of the above four particles with different sizes.

Particle size	4 nm	6 nm	11.5 nm	14 nm
Misfit δ	< 5.03%	9.57%	22.9% / 22.3%	25.4% / 25.8%

Table 6
The average mechanical properties of 14Cr-ODS and 14Cr-Zr-ODS at room temperature (RT), 300 °C, 550 °C and 750 °C.

	Composition	YS (MPa)	UTS (MPa)	UE (%)
RT	14Cr-ODS	750.6 ± 14.0	903.6 ± 16.0	11.4 ± 0.6
	14Cr-Zr-ODS	816.3 ± 30.0	994.3 ± 9.5	13.0 ± 1.3
300 °C	14Cr-ODS	594.6 ± 17.2	731.0 ± 6.6	11.8 ± 0.9
	14Cr-Zr-ODS	620.3 ± 11.8	752.6 ± 8.0	13.9 ± 1.0
550 °C	14Cr-ODS	342.4 ± 14.7	358.3 ± 10.3	16.3 ± 0.7
	14Cr-Zr-ODS	374.6 ± 9.3	405.3 ± 7.6	22.6 ± 0.4
750 °C	14Cr-ODS	84.6 ± 12.3	98.1 ± 11.6	24.1 ± 1.2
	14Cr-Zr-ODS	127.3 ± 13.1	139.6 ± 7.6	30.3 ± 0.9

14Cr-ODS samples. It indicates that the addition of Zr can significantly improve the mechanical properties of ODS steels at both room and high temperatures. With the temperature increasing from room temperature to 750 °C, the strength of these two ODS steels continuously decrease (from 750.6 MPa to 84.6 MPa in average YS and from 903.6 MPa to 98.1 MPa in average UTS for 14Cr-ODS, from 816.3 MPa to 127.3 MPa in average YS and from 994.3 MPa to 139.6 MPa in average UTS for 14Cr-Zr-ODS). The UE of these two ODS steels have an obvious increasing overall trend with the temperature increasing. When the temperature rises to 750 °C, the UE of 14Cr-ODS and 14Cr-Zr-ODS reach about 24% and 30% respectively.

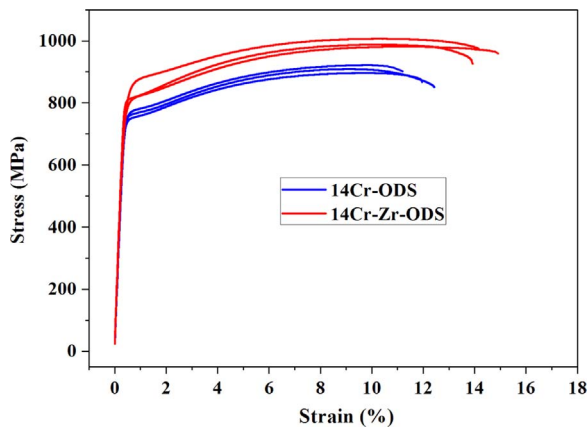**Fig. 10.** Tensile stress-strain curves tested at room temperature for the two contrast steels of 14Cr-ODS and 14Cr-Zr-ODS.

3.2.2. Strengthening mechanism of Zr addition

The strengthening mechanism of Zr addition in the ODS steels can be explained mainly by load partition phenomenon and particle-dislocation interactions at both room and high temperatures.

3.2.2.1. Load partition phenomenon. The load partition phenomenon [22,23] indicates that the oxide particles take more loads than the matrix during the plastic deformation process. In ODS steels, the low interface energy of the well coherent particles can not only prevent coarsening of the particles by reducing the Gibbs-Thomson effect at the interface, but also improve the bonding force between the particles and the matrix [19]. Fig. 12(a) and (b) shows the SEM images of the fracture surfaces of 14Cr-ODS and 14Cr-Zr-ODS respectively. It can be seen from Fig. 12(a) that large particles present in some dimples on the fracture surface, which indicates that the failure occurs in the interface between large particles and their matrix due to the poor interface bonding force. In other words, these interfaces fractured during the stage of plastic deformation and these extreme large particles in 14Cr-ODS did not take much loads during plastic deformation. Moreover, some cleavage steps are also observed in Fig. 12(a). The coexistence of both dimples and cleavage steps in the fracture surface indicates that the 14Cr-ODS shows
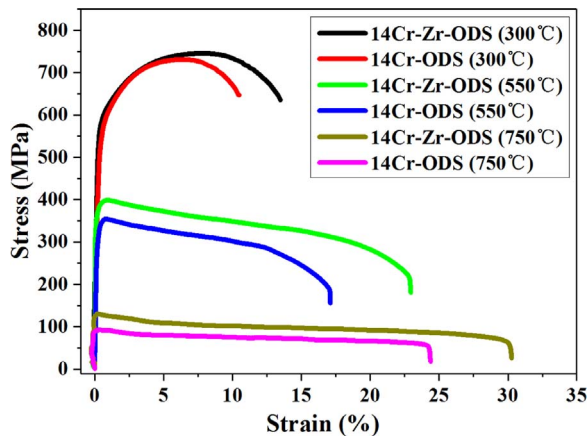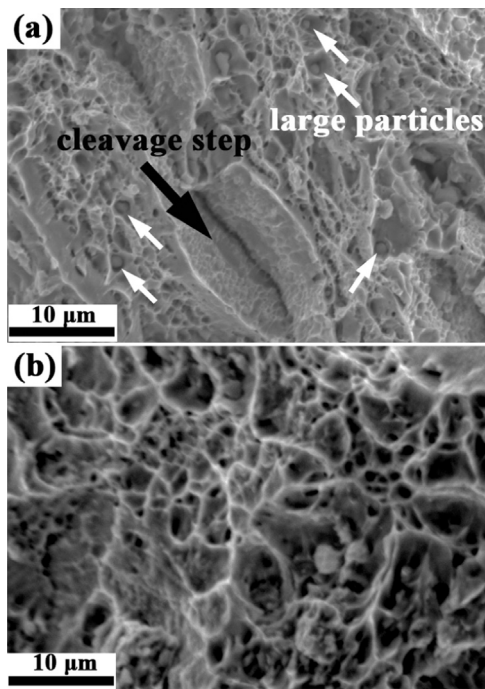

Fig. 11. Average tensile stress-strain curves tested at various high temperatures (300, 550 and 750 °C) for the two contrast steels of 14Cr-ODS and 14Cr-Zr-ODS.

measured at high temperatures are shown in Fig. 11. The average yield strength (YS), ultimate tensile strength (UTS) and uniform elongation (UE) of 14Cr-ODS and 14Cr-Zr-ODS samples are summarized in Table 6.

It can be seen that, at all four test temperatures, 14Cr-Zr-ODS samples exhibit higher YS and UTS and superior UE compared with

Fig. 12. SEM micrographs of fractured section surface of (a) 14Cr-ODS and (b) 14Cr-Zr-ODS after tensile.

a mixed ductile and brittle fracture. Unlike the 14Cr-ODS, the fracture of the 14Cr-Zr-ODS shows only regular shaped dimples covering the entire fractured surface, as seen in Fig. 12(b), which indicates a pure ductile fracture. The difference in the fracture surface characteristics between those two alloys is the primary reason why the 14Cr-Zr-ODS alloy exhibits superior mechanical properties in the uniaxial tensile tests, as shown in Figs. 10 and 11. The strong interface bonding force of small coherent $Y_4Zr_3O_{12}$ particles can prevent the failure on the interface and improve the tensile strength and elongation of ODS steels.

3.2.2.2. Particle-dislocation interactions. It is well known that the plastic deformation is associated primarily with the dislocation movement. Therefore, any factors that can effectively interfere with the dislocation movement will contribute to mechanical property enhancement. In ODS steels, the nano-sized oxide particles dispersed in the matrix play a crucial role in dislocations pinning. In generally, the dislocations overcome the pinning effect of nanoparticles through two mechanisms: Orowan looping ($r_{particle} > r_{crit}$) and shearing ($r_{particle} < r_{crit}$). Since the critical radius r_{crit} in the ferritic matrix is about 2 nm [24], the dominant depinning mechanism in the present samples can be assumed to be the Orowan looping mechanism considering the fact that the size of almost all the oxide particles are larger than 2 nm (see Fig. 2(c)).

Fig. 13 shows the TEM image of the 14Cr-Zr-ODS sample after tensile deformation. It is observed that several dislocations are obstructed by dispersed particles, which indicates the occurrence of particle-dislocation interactions during deformation. In this process, a dislocation will first bow and pass through a state of the maximum energy (the saddle-state), and then bypass the particle and leave a dislocation loop around the particle. The saddle-state can be illustrated by the schematic diagram shown in Fig. 13 and the shear stress needed by dislocation to pass through this threshold is called critical resolved shear stress (CRSS). Here the CRSS will be calculated in order to compare the pinning effects of the oxide particles in the 14Cr-ODS and the 14Cr-Zr-ODS. For edge dislocations, the CRSS (τ_{loop}) can be approximated by:
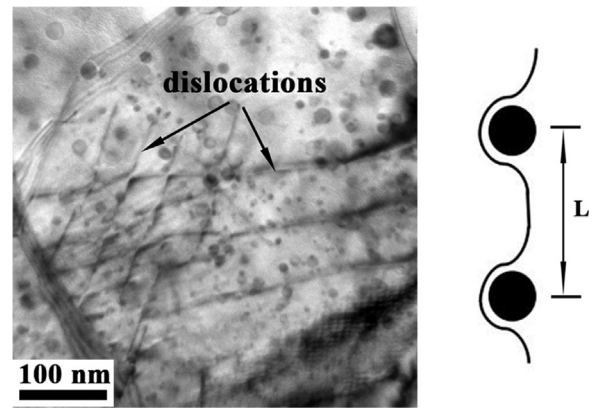

Fig. 13. TEM image of particle-dislocation interactions in 14Cr-Zr-ODS after tensile, and the schematic diagram of saddle-state for a dislocation bypassing particles.

$$\tau_{loop} = \frac{2 - \nu}{4(1 - \nu)} \frac{Gb}{2L - \pi r}\left[\ln\left(\frac{4r}{\rho}\right) - 2\right],\tag{4}$$

where ν is the Poisson ratio, G is the shear modulus, b is the Burgers vector, L is the inter-particle spacing (the distance between the centers of two particles), r is the average radius of particles and ρ is an effective dislocation core radius [25]. The CRSS associated with a screw dislocation can be obtained from the CRSS in the above equation for an edge dislocation divided by a factor $(1-\nu)$. For the ODS steels in the present work, $G \approx 79$ GPa, $\nu = 0.27$, $b = a_0 / \sqrt{2}$ with $a_0 = 2.87$ Å and $\rho = 1.165b$. According to Eq. (4) and the statistical results in Table 2, the nanoparticles distributions in the 14Cr-ODS and the 14Cr-Zr-ODS would lead to critical stresses of 1148 MPa and 1526 MPa respectively for the edge dislocations. For screw dislocations, their corresponding critical stresses would be 1572 MPa and 2090 MPa, respectively. Although the above calculated theoretical values may not perfectly match with the actual tested values due to a series of factors not considered in the calculation model, these results still prove that more fine and homogeneous particles would produce more contribution to pinning effects of the dislocations and result in a more excellent tensile strength in the 14Cr-Zr-ODS alloys.

The two performance enhancement mechanisms discussed above are applicable not only to room temperature but also to high temperatures. In fact, the high-temperature mechanical properties of ODS steels mainly depend on the thermal stability of the oxide particles. And the thermal stability of the oxide particles is associated with the strong structural affinity with the matrix to a great extent. In the 14Cr-Zr-ODS, the smaller sized $Y_4Zr_3O_{12}$ particles are more coherent with surrounding matrix, and the orderly interface between them has lower interface energy. When ODS steels are in service under high heat load, the $Y_4Zr_3O_{12}$ particles can possess excellent coarsening resistance and maintain their small sizes and homogeneous distribution. So these fine and thermal-stable particles can play a stronger role in pinning dislocation movements, and their stronger interfacial bonding force can reduce failure at particle surface under high temperatures and finally improve the comprehensive performance of ODS steels. In addition, these densely dispersed nano-sized oxide particles can also prevent helium swelling by providing the formation sites of little helium bubbles, and thus improve the radiation damage resistance of ODS steels under neutron fluxes environment.

4. Conclusions

In this study, the influences of Zr addition on the microstructures and mechanical properties of ODS steels were investigated. The conclusions are summarized as follows:

(1) The precipitated oxide particles in the 14Cr-Zr-ODS have smaller

sizes, higher number density, and disperse more uniformly in the matrix than those in the 14Cr-ODS. That is because many finer rhombohedral $Y_4Zr_3O_{12}$ particles were formed in the ODS steels with Zr addition.

(2) Most of the oxide particles in the 14Cr-Zr-ODS are coherent or semi-coherent with the matrix. The particle-matrix interface misfit δ increases as the particle size increases. When the particle size is too large, the crystal planes of the particle and the matrix are no longer completely paralleled under the direction of active vector **g**.

(3) The addition of Zr can effectively improve the yield and tensile strength of ODS steel and improve the ductility. The strengthening mechanisms with the Zr addition include the stronger interface bonding force between fine precipitated particles and matrix and the larger pinning effect of small particles on dislocation movements.

Acknowledgments

References

[1] V. de Castro, E.A. Marquis, S. Lozano-Perez, R. Pareja, M.L. Jenkins, Acta Mater. 59 (2011) 3927–3936.

[2] M. Laurent-Brocq, F. Legendre, M.H. Mathon, A. Mascaro, S. Poissonnet, B. Radiguet, P. Pareige, M. Loyer, O. Leseigneur, Acta Mater. 60 (2012) 7150–7159.

[3] X. Hu, L. Huang, W. Yan, W. Wang, W. Sha, Y. Shan, K. Yang, Mater. Sci. Eng.: A 586 (2013) 253–258.

[4] S. Liu, Q. Huang, L. Peng, Y. Li, C. Li, Fusion Eng. Des. 87 (2012) 1628–1632.

[5] J.-H. Gwon, J.-H. Kim, K.-A. Lee, J. Nucl. Mater. 459 (2015) 205–216.

[6] I. Hilger, M. Tegel, M.J. Gorley, P.S. Grant, T. Weißgärber, B. Kieback, J. Nucl. Mater. 447 (2014) 242–247.

[7] S. Ohtsuka, T. Kaito, M. Inoue, T. Asayama, S.W. Kim, S. Ukai, T. Narita, H. Sakasegawa, J. Nucl. Mater. 386–388 (2009) 479–482.

[8] S. Takaya, T. Furukawa, G. Müller, A. Heinzel, A. Jianu, A. Weisenburger, K. Aoto, M. Inoue, T. Okuda, F. Abe, S. Ohnuki, T. Fujisawa, A. Kimura, J. Nucl. Mater. 428 (2012) 125–130.

[9] Y. Miao, K. Mo, B. Cui, W.-Y. Chen, M.K. Miller, K.A. Powers, V. McCreary, D. Gross, J. Almer, I.M. Robertson, J.F. Stubbins, Mater. Charact. 101 (2015) 136–143.

[10] H. Kotan, K.A. Darling, R.O. Scattergood, C.C. Koch, J. Alloy. Compd. 615 (2014) 1013–1018.

[11] R. Gao, T. Zhang, X.P. Wang, Q.F. Fang, C.S. Liu, J. Nucl. Mater. 444 (2014) 462–468.

[12] R. Rahmanifard, H. Farhangi, A.J. Novinrooz, J. Alloy. Compd. 622 (2015) 948–952.

[13] C.Z. Yu, H. Oka, N. Hashimoto, S. Ohnuki, J. Nucl. Mater. 417 (2011) 286–288.

[14] S. Ohnuki, N. Hashimoto, S. Ukai, A. Kimura, M. Inoue, T. Kaito, T. Fujisawa, T. Okuda, F. Abe, in: Proceedings of the ICAPP 2009, Tokyo, Japan, 2009. Article ID. 9306.

[15] H. Oka, M. Watanabe, N. Hashimoto, S. Ohnuki, S. Yamashita, S. Ohtsuka, J. Nucl. Mater. 442 (2013) S164–S168.

[16] P. Dou, A. Kimura, R. Kasada, T. Okuda, M. Inoue, S. Ukai, S. Ohnuki, T. Fujisawa, F. Abe, J. Nucl. Mater. 444 (2014) 441–453.

[17] M.F. Ashby, L.M. Brown, Philos. Mag. 8 (1963) 1083–1103.

[18] P. Dou, A. Kimura, T. Okuda, M. Inoue, S. Ukai, S. Ohnuki, T. Fujisawa, F. Abe, J. Nucl. Mater. 417 (2011) 166–170.

[19] J. Ribis, Y. de Carlan, Acta Mater. 60 (2012) 238–252.

[20] X. Mao, K.H. Oh, S.H. Kang, T.K. Kim, J. Jang, Acta Mater. 89 (2015) 141–152.

[21] H. Liu, J. Civil. Aviat. Inst. China 13 (1995) 54–58.

[22] Y. Miao, K. Mo, Z. Zhou, X. Liu, K.-C. Lan, G. Zhang, M.K. Miller, K.A. Powers, J. Almer, J.F. Stubbins, Mater. Sci. Eng.: A 625 (2015) 146–152.

[23] K. Mo, Z. Zhou, Y. Miao, D. Yun, H.-M. Tung, G. Zhang, W. Chen, J. Almer, J.F. Stubbins, J. Nucl. Mater. 455 (2014) 376–381.

[24] Y.N. Osetsky, D.J. Bacon, J. Nucl. Mater. 323 (2003) 268–280.

[25] L. Proville, B. Bakó, Acta Mater. 58 (2010) 5565–5571.